

Diamond mirrors for high-power lasers

H. Atikian¹, N. Sinclair^{1,2}, P. Latawiec¹, X. Xiong^{1,3}, S. Meesala¹, S. Gauthier¹, D. Wintz¹, J. Randi⁴, D. Bernot⁴, S. DeFrances⁴, J. Thomas⁴, M. Roman⁵, S. Durrant⁵, F. Capasso¹, and M. Lončar^{1*}

¹John A. Paulson School of Engineering and Applied Sciences, Harvard University, Cambridge, MA 01238, USA.

²Division of Physics, Mathematics and Astronomy, and Alliance for Quantum Technologies (AQT), California Institute of Technology, Pasadena, CA 91125, USA. ³Key Laboratory of Quantum Information and Synergetic Innovation Center of Quantum Information and Quantum Physics, University of Science and Technology of China, Hefei, Anhui 230026, China. ⁴Pennsylvania State University Applied Research Laboratory, Electro-Optics Center, Freeport, PA 16229, USA. ⁵Laser Technology and Analysis Branch, Naval Surface Warfare Center, Dahlgren Division, Dahlgren, VA 22448, USA. *e-mail: loncar@seas.harvard.edu

High-power lasers have numerous scientific and industrial applications. Some key areas include laser cutting and welding in manufacturing¹⁻⁴, directed energy in fusion reactors or defense applications⁵⁻⁸, laser surgery in medicine⁹, and advanced photolithography in the semiconductor industry^{10,11}. These applications require optical components, in particular mirrors, that withstand high optical powers for directing light from the laser to the target. Ordinarily, mirrors are comprised of multilayer coatings of different refractive index and thickness. At high powers, imperfections in these layers lead to absorption of light, resulting in thermal stress and permanent damage to the mirror. Here we design, simulate, fabricate, and demonstrate monolithic and highly reflective dielectric mirrors which operate under high laser powers without damage. The mirrors are realized by etching nanostructures into the surface of single-crystal diamond, a material with exceptional optical and thermal properties. We measure reflectivities of greater than 98% and demonstrate damage-free operation using 10 kW of continuous-wave laser light at 1070 nm, with intensities up to 4.6 MW/cm². In contrast, at these laser powers, we observe damage to a standard dielectric mirror based on optical coatings. Our results initiate a new category of broadband optics that operate in extreme conditions.

Modern dielectric mirrors use multi-layered coatings¹² or nanostructured thin films¹³ to engineer their reflection spectrum. The former utilizes alternating thin-film layers of varying refractive index and thickness to generate an interference effect at a desired wavelength and polarization, while the latter leverages localized or guided resonances to achieve high reflectivity. Yet, imperfections and defects in, or interfaces between, thin films form sites where laser energy can be absorbed¹⁴⁻¹⁷. At high laser powers, absorption at these sites generates significant heat, causing melting or thermal stress between film layers. This degrades the optical performance and produces irreversible damage to the mirror. We overcome this limitation of multilayered, multi-material, optical coatings by engineering the optical response of diamond and demonstrate it as a highly reflective mirror for high-power lasers. Diamond is employed due to its exceptional properties: relatively high refractive index (2.4), wide bandgap (5.5 eV), high mechanical hardness and chemical resistance, and possessing the highest material thermal conductivity at room temperature (2200 W/K·m)¹⁸⁻²⁰. Consequently, diamond optics offer use in diversified applications and operating environments.

Photonic crystals and metamaterials have emerged as a promising technology for tailoring properties of optical beams²¹⁻²⁵. These are typically composed of two-dimensional arrays of holes or rods in a thin-film layer that allow engineering the spatial distribution of amplitude, phase, and polarization response of an

optical element²⁶⁻²⁹. Many optical components have been realized using this approach, such as mirrors, lenses, and polarization optics³⁰⁻³⁵. Conventionally, planar photonic crystals and metamaterials are formed by nanopatterning a high-index dielectric (or metallic) film that has been deposited on a low-index substrate to leverage the index contrast needed to support optical resonances^{36,37}. Yet, these suffer from the same power handling limitations as conventional multilayer thin films. We avoid this by fashioning nanostructured mirrors from a monolithic substrate (with exceptional properties).

As illustrated in Fig. 1A, a mirror is formed by a planar lattice of identical “golf tee”-shaped columns that are etched into a diamond surface. For comparison, Fig. 1B depicts a traditional multilayered optical coating on a substrate. It is possible to control the properties of the mirror by engineering the geometry of each column in the lattice. Referring to Fig. 1C, this involves varying the angle α of the top region, radii r_{disc} , r_{min} , $r_{support}$, column height h , and the pitch, i.e. the center-to-center distance between the columns. The high reflectivity of the structure is attributed to a lattice resonance that is dominated by lateral leaky Bloch modes³⁸. These guided resonances are confined to the top region of each column, as seen in Fig. 1E, and are not supported by the narrowest part of the column which facilitates mode confinement. To achieve reflection, parameters of the periodic array must satisfy the well-known grating equation $d(\sin \theta_i - \sin \theta_m) = m\lambda$, where d is the grating period or pitch, m is an integer representing the diffraction order, the angles of the incident beam and the m th diffracted order are θ_i and θ_m , while λ is the wavelength of the incident beam³⁹. The first diffraction orders are coupled into the resonance supported by the top portion of the column, and then out-couple to the zeroth order of the grating in both reflected and transmitted direction. With proper design of the columns, incident angle and wavelength of light, the transmitted beams will interfere destructively resulting in perfect reflection, as indicated by the uniform phase front above the mirror in Fig. 1E.

Intuitively, the lateral mode guiding can be understood in the following way. Each column comprises three distinct regions of effective refractive index, labeled n_1 , n_2 , and n_3 in Fig. 1C. The shaded red region labeled n_2 contains the top region of the column. It effectively acts as the high-index layer since it contains more diamond per volume than the other regions and serves as the guiding layer for supporting leaky Bloch mode resonances in the device. The shaded yellow region labeled n_3 contains the narrow parts of the column, thereby acts as a lower-index layer ($n_3 < n_2$), and will provide optical confinement for the guiding layer n_2 . The shaded yellow region above labeled n_1 is air, providing the condition that the effective indices of each region $n_2 > n_1$, $n_3 > n_1$ to support guided optical resonances^{40,41}.

Simulations using a finite-difference time-domain (FDTD) solver, are performed to optimize the structure for maximum reflection at vertical incidence. Figure 1D shows a simulated diamond mirror reflection spectrum for varying design angles α . We target an operating wavelength of 1064 and 1070 nm, which are technologically relevant for high power lasers, while dimensions of the columns are chosen to give the widest bandwidth of high reflectivity around the target wavelength, see Fig. 1D. More details on the FDTD simulations and reflection spectra for other relevant dimensions are described in Supplementary Discussion 1.

To realize these complex 3-D structures across a wide area, we develop an unconventional, yet scalable, angled-etching nanofabrication technique for single-crystal diamond, as illustrated in Fig. 2 and described in its caption. Concisely, we utilize oxygen-based reactive-ion beam angled etching (RIBAE)⁴². Complete fabrication details are discussed in the Methods.

An optical image of a fabricated mirror is shown in Fig. 2B. A scanning electron microscope (SEM) image of the mirror is presented in Fig. 2C, with a zoomed image displayed in Fig. 2D. Both images show the “golf tee”-shaped columns in a uniformly spaced array. The area of the diamond mirror is 3 mm x 3 mm, with nearly identical device geometry from one edge of the mirror to the other. The ability to precisely,

and uniformly, fabricate nanometer-scale geometries across a large surface is enabled by the RIBAE technique.

The reflection spectrum of a diamond mirror is measured using a procedure outlined in the Methods. The result is shown in Figure 3A, showing excellent agreement with the predictions of the FDTD simulations for $\alpha = 70^\circ$ and the rest of our target design parameters, see the caption of Fig. 1D. An absolute reflectivity of $98.9 \pm 0.3\%$ at 1064 nm is measured, with uncertainty owing to the accuracy of the optical power detector. Approximately 0.5% of the optical power is transmitted through the backside-polished diamond substrate, while the remaining 0.6% is loss, likely due to scatter rather than absorption. Measurements of high-Q resonators produced in diamond using RIBAE have suggested little surface absorption⁴²⁻⁴⁴. Moreover, a reflectivity of greater than 98% is observed across a 10 nm bandwidth around 1064 nm, also consistent with simulations.

Beam profile measurements are performed on the reflection from the diamond mirror to ensure an incident 1064 nm-wavelength Gaussian beam is not distorted. See the Methods for more details. A 2-D plot of the power distribution of the reflected beam is presented in Fig. 3B, with cross-sectional profiles for each axis overlaid with an independent Gaussian fit. These measurements are used to determine the 3-D power distribution of the reflected beam, as depicted in the inset of Fig 3B, further illustrating the absence of any beam distortion. Note that our FDTD simulations show that the nanostructured diamond surface maintains a uniform phase-front for reflected beams, see Supplementary Fig. 6.

Next, we design and fabricate a 3 mm x 3 mm mirror with measured reflectivity of 96% at 1070 nm, water-cool it to 18°C, and, by irradiating it for 30 s with varied laser powers, assess its laser induced damage threshold (LIDT) at this wavelength. Note that typical optics use beam expanders to mitigate laser damage, while here we focus the beam to a $750 \mu\text{m}$ ($1/e^2$) diameter, corresponding to hundreds of periods of the “golf-tee” lattice. Thus, we ensure the irradiance is maximized (up to 4.6 MW/cm^2) to provide optimal conditions for potential damage. Optical and thermal images taken during the LIDT tests are shown in Figs. 4A-E, while all details of the testing mirror, setup, and procedure are provided in the figure caption and Methods. Thermal and optical videos of the tests are shown in Supplementary Videos 1-6. The hot spot in the images suggests that 4% of laser power is transmitted through the mirror, heating the underlying water-cooled stage. Images of the mirror under varying SEM magnification, see Fig. 4F for a wide-angle view, and using an optical microscope after the tests indicate no damage or change in surface morphology. Moreover, we measured the mirror reflectivity after the tests, finding that it was also maintained. Therefore, we could not determine the LIDT for the diamond mirror with illumination using up to 10 kW of laser power, demonstrating its robustness for high power applications.

To put our result into context, we repeat the LIDT tests using a standard dielectric mirror of 99.5% reflectivity. Optical and thermal images are shown in Figs. 4G-K, with further details of the testing, dielectric mirror properties, and setup described in the figure caption and Methods, while a thermal video of the test at 10 kW power is shown in Supplementary Video 7. As the power is increased, the hot spot rapidly increases in temperature due to absorption, poor thermal conductivity, and expansion of the dielectric coatings¹⁶, leading to damage under 10 kW of irradiation. This is confirmed by an optical image of the mirror taken after the tests, shown in Fig. 4L, which suggests inferior performance to the diamond mirror for high power optics.

We demonstrated highly reflective monolithic diamond mirrors that withstand high laser power. Our results are supported by beam profile measurements and numerical modeling in which no distortions in the reflected laser beam were inferred. Damage testing demonstrated the ability the mirrors to operate under high-power laser illumination, contrary to that using a standard dielectric mirror. We expect our work to stimulate development of a new class of optical components for high-power laser applications across the optical spectrum. For example, applications in directed energy or extreme ultraviolet

lithography systems that utilize high power CO₂ lasers will benefit^{10,11}. Finally, we emphasize that our mirror technology is not limited to diamond alone, as reflectors can be fabricated from a wide variety of substrates. For example, monolithic mirrors leveraging the extremely large bandgap (~9 eV) of fused silica could benefit ultrafast laser applications, where the damage mechanism is dominated by dielectric breakdown.

References

1. Nilsson, J. & Payne, D. N. High-power fiber lasers. *Science* **332**, 921-922 (2011).
2. Jackson, S. D. Towards high-power mid-infrared emission from a fibre laser. *Nat. Photon.* **6(7)**, 423-431 (2012).
3. Crafer, R. & Oakley, P. J. Laser processing in manufacturing. *Springer* (2013).
4. Penilla, E. H., et al. Ultrafast laser welding of ceramics. *Science* **365**, 803-808 (2019).
5. Dunne, M. A high-power laser fusion facility for Europe. *Nat. Phys.* **2** (1), 2-5 (2006).
6. Clery, D. Laser fusion reactor approaches 'burning plasma' milestone. *Science* **370**, 1019-1020 (2020).
7. Norreys, P. A. Complexity in fusion plasmas. *Science* **319**, 1193-1194 (2008).
8. Nuckolls, J., Wood, L., Thiessen, A., & Zimmerman, G. Laser compression of matter to super-high densities: Thermonuclear (CTR) applications. *Nature* **239**, 139-142 (1972).
9. York, P. A., Peña, R., Kent, D. & Wood, R. J. Microrobotic laser steering for minimally invasive surgery. *Science Robotics* **6**, 50 (2021).
10. Tallents, G., Wagenaars, E. & Pert, G. Optical lithography: Lithography at EUV wavelengths. *Nat. Photon.* **4**, 809 (2010).
11. Fomenkov, I., Schafgans, A., & Brandt, D. Laser-Produced Plasma Sources for High-Volume-Manufacturing EUV Lithography. *Synchrotron Radiation News* **32** (4), 3-8 (2019).
12. Baumeister, P. W. Optical coating technology. *Optimization* **10**, 7 (2004).
13. Fan, S. & Joannopoulos, J. D. Analysis of guided resonances in photonic crystal slabs. *Phys. Rev. B* **65**, 235112 (2002).
14. Taylor, L. N., Brown, A. K., Pung, A. J., Johnson, E. G., Talghader, J. J. Continuous-wave laser damage of uniform and nanolaminate hafnia and titania optical coatings. *Opt. Lett.* **38**, 4292-4295 (2013).
15. Ristau, D. Laser-Induced Damage in Optical Materials. *CRC Press* (2014).
16. Ristau, D., Jupé, M., Starke, K. Laser damage thresholds of optical coatings. *Thin Solid Films* **518**, 1607-1613 (2009).
17. Tumkur, T. U., et al. Toward high laser power beam manipulation with nanophotonic materials: evaluating thin film damage performance. *Optics Express* **29** (5), 7261-7275 (2021).
18. Brierley, C.J., Beck, C. M., Kennedy, G. R., Metcalfe, J., Wheatley, D. The potential of CVD diamond as a replacement to ZnSe in CO₂ laser optics. *Diamond and Related Materials* **8**, 1759-1764 (1999).
19. Zaitsev, A. M. Optical Properties of Diamond A Data Handbook. *Springer* (2001).
20. Mildren, R. "Chapter 1: Intrinsic properties of diamond" in Mildren, R. & James R., Optical engineering of diamond. *John Wiley & Sons* (2013).
21. Cai, W. & Shalaev, V. Optical Metamaterials: Fundamentals and Applications. *Springer* (2009).
22. Engheta, N. & Ziolkowski, R. W. Metamaterials: Physics and Engineering Explorations. *Wiley-IEEE* (2006).
23. Pendry, J. B., Schurig, D., & Smith, D. R. Controlling Electromagnetic Fields. *Science* **312**, 1780 (2006).
24. Yu, N. & Capasso, F. Flat optics with designer metasurfaces. *Nat. Mater.* **13**, 139-150 (2014).
25. Dory, C., et al. Inverse-designed diamond photonics. *Nat. Comm.*, **10** (1), 1-7 (2019).
26. Aieta, F., Kats, M. A., Genevet, P., Capasso, F. Multiwavelength achromatic metasurfaces by dispersive phase compensation. *Science* **347**, 1342 (2015).
27. Esfandyarpour, M. Garnett, E. C., Cui, Y., McGehee, M.D., Brongersma, M. L. Metamaterial mirrors in optoelectronic devices. *Nat. Nano.* **9**, 542-547 (2014).

28. Kildishev, A. V., Boltasseva, A., Shalae, V. M. Planar Photonics with Metasurfaces. *Science* **339**, 6125 (2013).
29. Arbabi, A., Horie, Y., Bagheri, M., Faraon, A. Dielectric metasurfaces for complete control of phase and polarization with subwavelength spatial resolution and high transmission. *Nat. Nano.* **10**, 937 (2015).
30. Khorasaninejad, M. & Capasso, F., Metalenses: Versatile multifunctional photonic components. *Science* **358**, 6367 (2017).
31. Khorasaninejad, M. et al. Metalenses at visible wavelengths: Diffraction-limited focusing and subwavelength resolution imaging. *Science* **352**, 1190 (2016).
32. Liu, S. et al. Optical magnetic mirrors without metals. *Optica* **1**, 250-256 (2014).
33. Moitra, P., Slovick, B. A., Gang Yu, Z., Krishnamurthy, S., Valentine, J. Experimental demonstration of a broadband all-dielectric metamaterial perfect reflector. *Appl. Phys. Lett.* **104**, 171102 (2014).
34. Moitra, P. et al. Large-Scale All-Dielectric Metamaterial Perfect Reflectors. *ACS Photonics* **2**, 692-698 (2015).
35. Slovick, B., Yu, Z. G., Berding, M., Krishnamurthy, S. Perfect dielectric-metamaterial reflector. *Phys. Rev. B* **88**, 165116 (2013).
36. Joannopoulos, J. D., Johnson, S. G., Winn, J. N., Meade, R. D. Photonic Crystals: Molding the Flow of Light, *Princeton University Press* (2008).
37. Wang, S. S. & Magnusson, R. Theory and applications of guided-mode resonance filters. *Appl. Opt.* **32**, 2606-2613 (1993).
38. Ko, Y. H. & Magnusson, R. Wideband dielectric metamaterial reflectors: Mie scattering or leaky Bloch mode resonance? *Optica* **5**, 289-294 (2018).
39. Rosenblatt, D., Sharon, A., Friesem, A. A. Resonant grating waveguide structures. *IEEE Journal of Quantum Electronics* **33**, 2038-2059 (1997).
40. Tibuleac, S. & Magnusson, R. Reflection and transmission guided-mode resonance filters. *J. Opt. Soc. Am. A* **14**, 1617-1626 (1997).
41. Bertoni, H. L., Cheo, L. h. S., Tamir, T. Frequency-selective reflection and transmission by a periodic dielectric layer. *IEEE Transactions on Antennas and Propagation* **37**, 78-83 (1989).
42. Atikian, H. A. et al. Freestanding nanostructures via reactive ion beam angled etching. *APL Photonics* **2**, 051301 (2017).
43. Bhaskar, M. K. et al. Experimental demonstration of memory-enhanced quantum communication. *Nature* **580**, 60-64 (2020).
44. Mitchell, M., Lake, D. P., & Barclay, P. E. Realizing $Q>300\,000$ in diamond microdisks for optomechanics via etch optimization. *APL Photonics*, **4** (1), 016101 (2019).

Acknowledgements

This work was performed in part at the Center for Nanoscale Systems (CNS), a member of the National Nanotechnology Coordinated Infrastructure Network (NNCI), which is supported by the National Science Foundation under NSF award no. 1541959. CNS is part of Harvard University. Laser-induced damage threshold of the diamond mirror was assessed at the Pennsylvania State University Applied Research Laboratory, Electro-Optics Center. This work was supported in part by the Air Force Office of Scientific Research (MURI, grant FA9550-14-1-0389), the Defense Advanced Research Projects Agency (DARPA, W31P4Q-15-1-0013), STC Center for Integrated Quantum Materials and NSF Grant No. DMR-1231319. N.S. further acknowledges support from the Natural Sciences and Engineering Research Council of Canada (NSERC), AQT Intelligent Quantum Networks and Technologies (INQNET) research program, the DOE/HEP QuantISED program grant, QCCFP (Quantum Communication Channels for Fundamental Physics), award number DE-SC0019219. P.L. was supported by the National Science Foundation

Graduate Research Fellowship under Grant No. DGE1144152. The authors thank Daniel Twitchen and Matt Markham from Element Six for their support with the diamond samples.

Author contributions

H.A. and M.L. conceived the idea. H.A., X.X., and S.G. performed simulations. H.A. fabricated the mirrors. S.M. assisted with diamond preparation. H.A. and P.L. designed the experiment setup. H.A. performed optical characterizations. D.W. assisted with beam profile measurements. H.A. and N.S. analyzed and interpreted the data. J. R., D. B., S. D., J. T., M. R., and S. D. assisted with laser damage testing. H.A. and N.S. wrote the manuscript with the help of all co-authors. F.C. and M.L. supervised the project.

Competing interests

H.A. and M.L. are inventors on patent applications related to this work (U.S. No.: 10,727,072, date filed: May 2016, granted: Jul 2020) and (U.S. Application No.: 15/759,909, date filed: Sept 2016). The authors declare that they have no other competing interests.

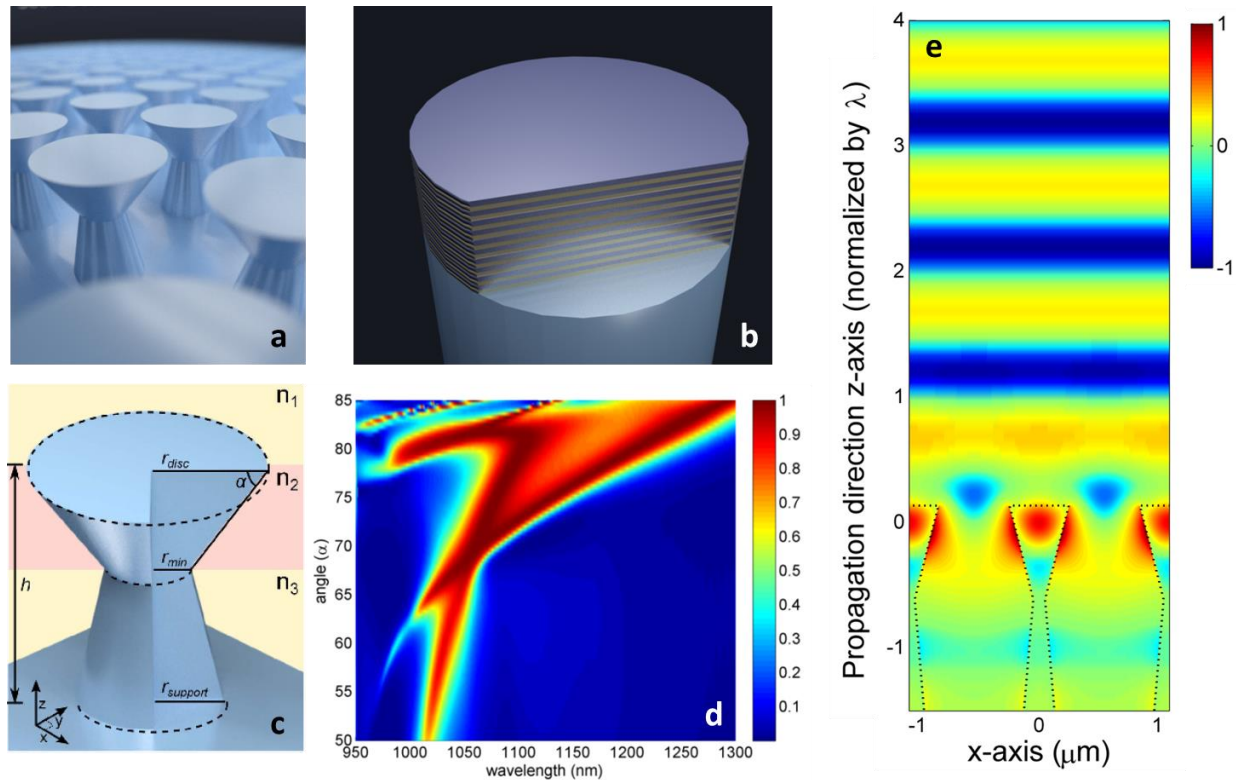


Fig. 1 | Diamond mirror design and simulation. **a**, Graphical depiction of a diamond mirror with the “golf tee”-shaped columns arranged in a hexagonal lattice. **b**, Typical multilayered optical coating deposited onto a substrate. **c**, Schematic of the “golf tee” columns that comprise the diamond mirror, with all relevant dimensions labeled: angle α , radii r_{disc} , r_{min} , $r_{support}$, and total height h . The shaded yellow region labeled n_1 is of lowest refractive index (air), the red region n_2 contains the top portion of the column that features optical resonances and is of highest refractive index, while the yellow region n_3 is of lower refractive index and supports the top portion of the column. **d**, Diamond mirror reflection spectrum at normal incidence for varying design angles α , with $r_{disc} = 250$ nm, $r_{min} = 50$ nm, $r_{support} = 250$ nm, pitch $1.1 \mu\text{m}$, and $h = 3 \mu\text{m}$. Colors indicate reflectivity. **e**, Standing-wave pattern illustrating the reflected wavefront from a diamond mirror at a wavelength of 1064 nm. Mode is confined in the top portion of the columns due to lattice resonance. Colors indicate the electric field amplitude. Photo Credit for panels A and B: P. Latawiec, Harvard.

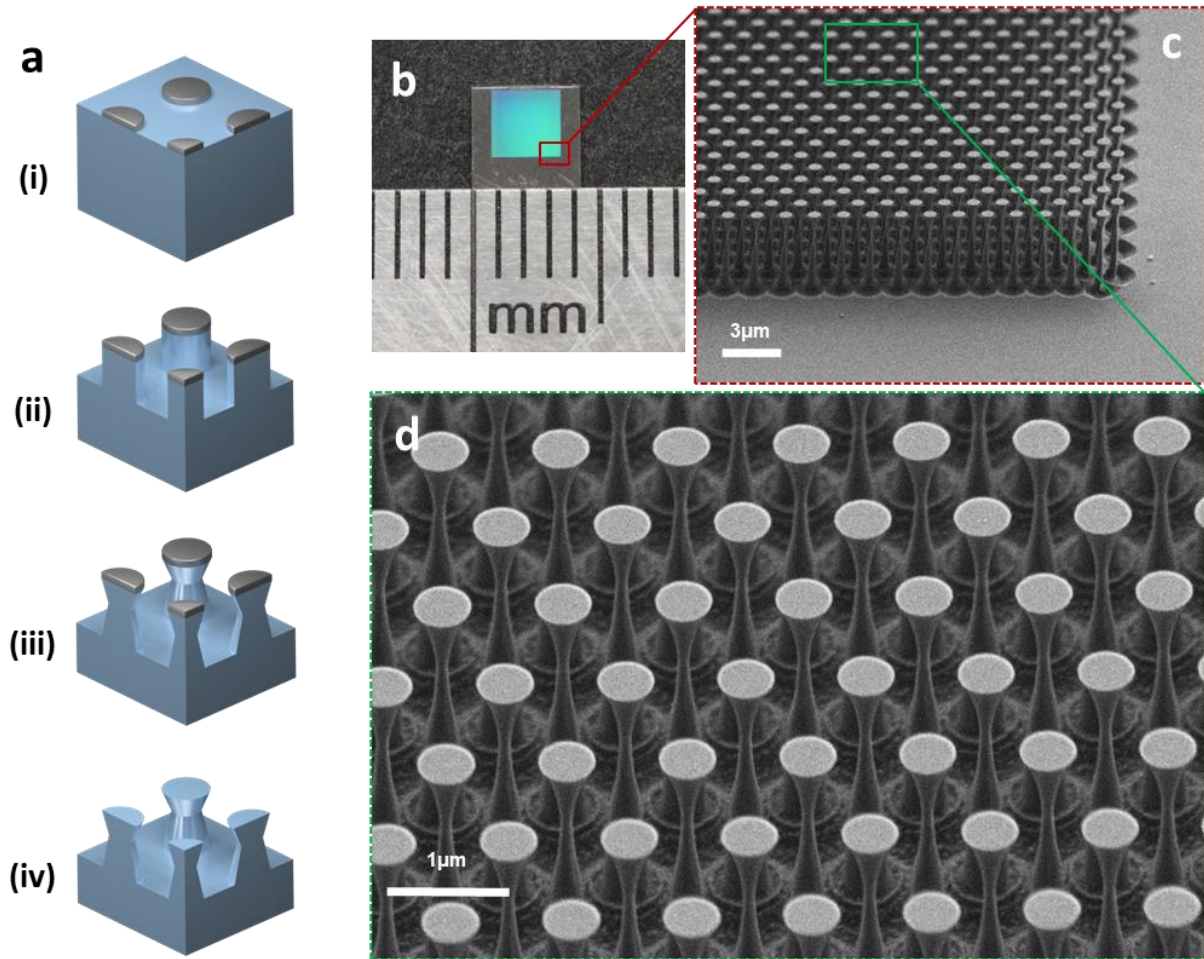


Fig. 2 | Diamond mirror fabrication and device images. **a**, Schematic of the reactive ion beam angled etching (RIBAE) fabrication process. (i) Etch mask is patterned onto the diamond sample surface. (ii) Top-down etch with the sample mounted perpendicular to the ion beam path on a rotating sample stage. (iii) Sample is tilted during etching to obtain the target angle α with respect to the direction of the ion beam, uniformly etching underneath the etch mask. (iv) Mask removal yields an array of 3-D nanostructures etched into the surface of diamond. **b**, Optical image of the diamond mirror on a 4.2 mm x 4.2 mm diamond crystal. Each division on the ruler is 1 mm. Photo Credit: H. Atikian, Harvard. **c**, SEM image of the diamond mirror taken at 60° from normal. **d**, Zoomed SEM image of the mirror taken at 40° from normal.

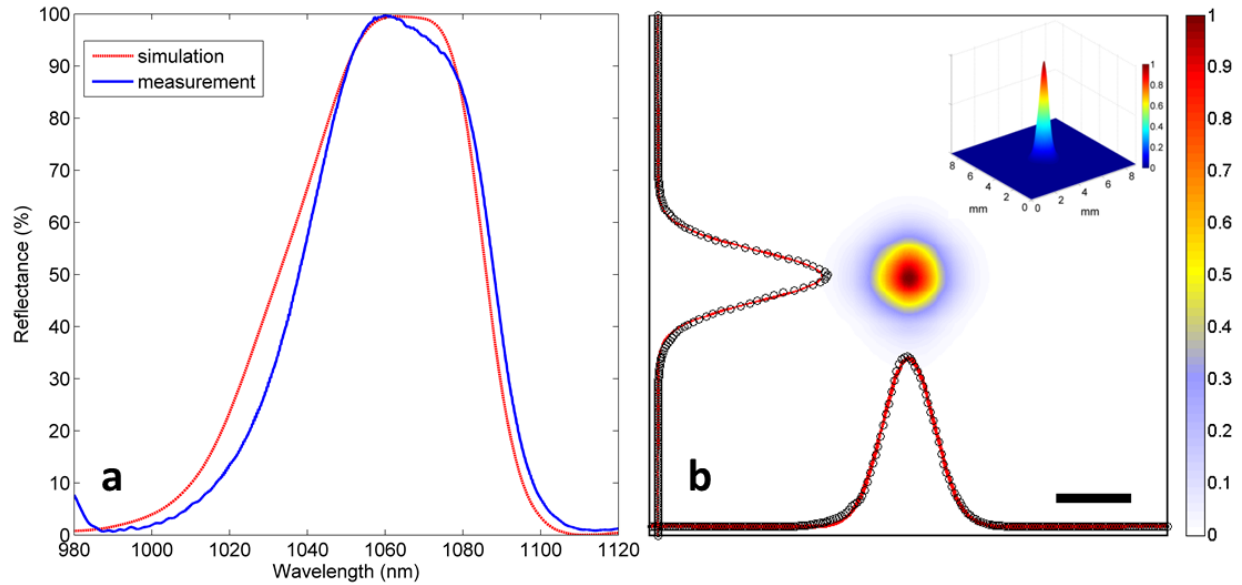


Fig. 3 | Optical characterization of a diamond mirror. **a**, Reflection spectrum of a diamond mirror, blue line is measurement data and red line is FDTD simulation. Absolute reflectivity of $98.9 \pm 0.3\%$ is measured at 1064 nm using a DBR laser. **b**, Beam profile measurement taken of the reflection from the diamond mirror using a scanning-slit profiler. Axes show cross sections of the reflected beam (black circles) with overlaid Gaussian fit (red). Fit yields a 4σ beam width of ~ 1.5 mm. Scale bar is 1 mm. Inset shows a 3-D perspective of the reflected beam. Colors indicate normalized optical power.

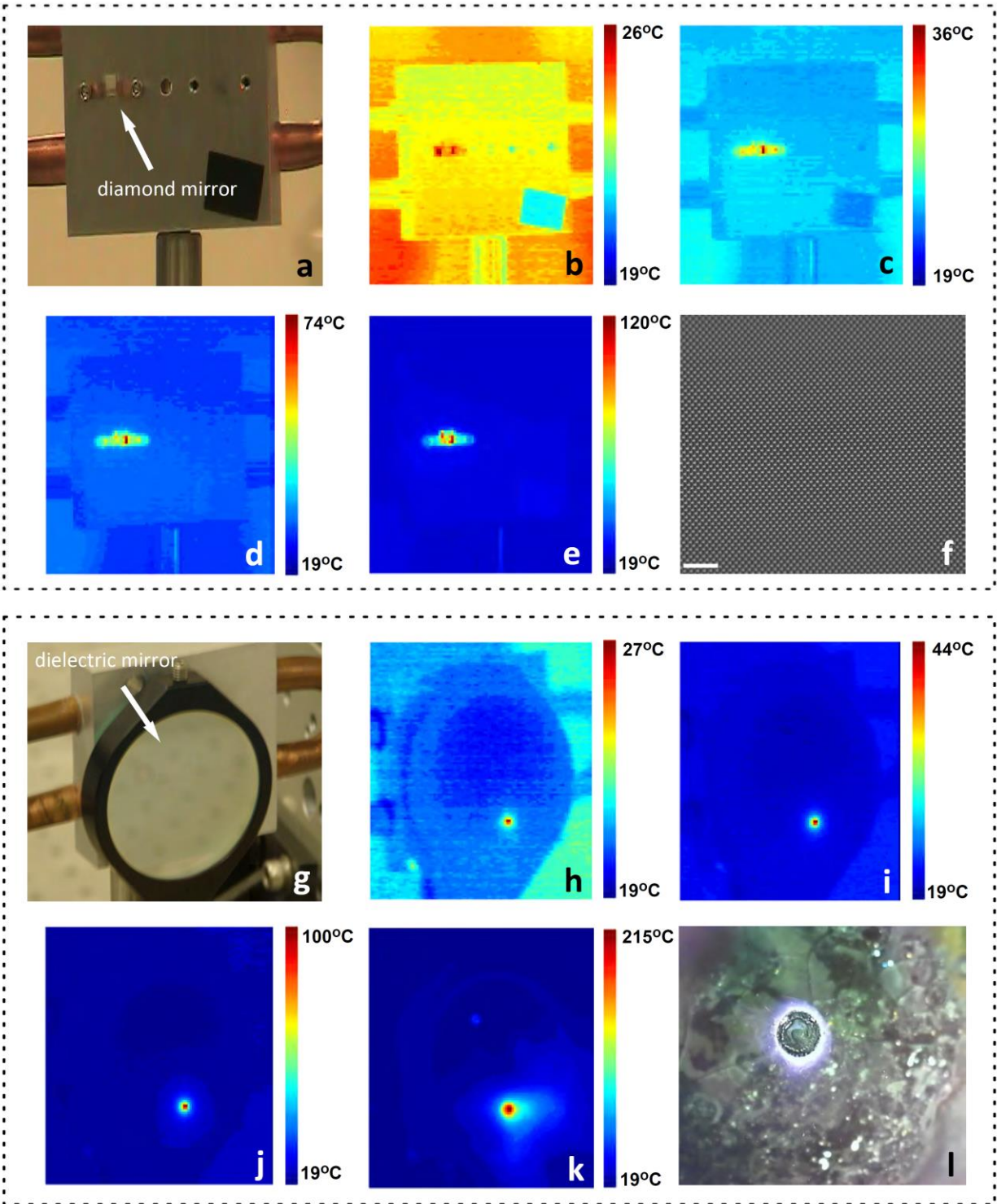


Fig. 4 | Laser induced damage testing of diamond (a-f) and dielectric (g-l) mirrors. a, Optical image of a diamond mirror mounted on a water-cooled stage that was taken prior to testing. **b-e**, Thermal images of the diamond mirror irradiated by 0.5, 2.5, 5, and 10 kW, respectively, of continuous-wave laser power. Color bar shows the temperature of the setup with varying scale for each image. Hot spot corresponds to the position of the beam (on the diamond mirror). At increased power levels a small fraction of

optical power leaking through the backside of the diamond mirror results in heating of the stage. **f**, Wide-area SEM image of the diamond mirror shows no damage after testing. Scale bar is 5 μm . **g**, Optical image of a corresponding dielectric mirror mounted on the water-cooled stage. **h-k**, Thermal images of the dielectric mirror irradiated by 0.5, 2, 6, and 10 kW, respectively, of CW laser power. Damage ensues at 10 kW of power due to thermal stress. **l**, Image of damage region of dielectric mirror taken after testing shows a several mm-sized hole where the laser beam ablated the dielectric. Photo Credit for panels A, G and L: S. DeFrances, Penn State EOC.

Methods

Diamond mirror fabrication. To realize the complex 3-D column structures across a wide area, we developed an unconventional, yet novel and scalable, angled-etching nanofabrication technique utilizing a reactive ion beam etching (RIBE) process. RIBE is a derivative of ion beam etching (IBE) in which a broad-area ion beam source is used to collimate and direct a beam of high energy ions from a gas source. The distinction of RIBE is that the plasma source is comprised of reactive gases, whereas IBE is limited to noble gases such as Ar, Xe, or Ne. We use O₂ as a reactive gas to etch diamond. Ions are extracted from the plasma source using a set of electrically biased grids typically made from Mo. Voltages applied to these grids, along with the plasma source, dictate the energy, flux, and divergence of the ions. Typically, the uniformity of the ion beam can be greater than 95% across the ion beam source diameter, and the size of the sample (e.g. wafer or crystal) to be processed is only restricted by the cross-section of the beam.

Extended Data Fig. 1 depicts the etching procedure that is used to create a diamond mirror, referred to as reactive ion beam angled etching (RIBAE)⁴². The process begins by patterning an etch mask onto the diamond surface followed by a top down etch with the sample mounted perpendicular to the ion beam path on a rotating sample stage, see Extended Data Fig. 1b(i). Once the desired etch depth has been reached, the sample is tilted to an angle α with respect to the path of the ion beam, and the diamond columns are uniformly undercut in all directions, see Extended Data Fig. 1b(ii). The etch mask is then removed to reveal the final structure depicted in Extended Data Fig. 1b(iii).

We now describe all steps of the fabrication process in detail. A mirror is created from a type IIa single-crystal diamond from Element 6, grown by chemical vapor deposition with less than 5 ppb nitrogen concentration. The diamond sample is cleaned in a boiling mixture of equal parts sulfuric, nitric, and perchloric acid^{42,43}. The etch mask is constructed as follows. First, a 70 nm-thick layer of Nb is deposited onto the surface of the sample by DC magnetron sputtering, followed by spin coating with hydrogen silsesquioxane (HSQ) resist. An array of circles in a hexagonal grid is created in the HSQ by performing 125 keV electron beam lithography following and developed using a 25% tetramethylammonium hydroxide solution. Finally, a top-down etch of the Nb film is performed in a UNAXIS Shuttleline inductively coupled plasma reactive ion etcher (ICP-RIE) with the following parameters: 400 W ICP power, 250 W radio frequency (RF) power, 40 sccm Ar flow rate, 25 sccm Cl₂ flow rate and 8×10^{-3} Torr process pressure.

The rest of the fabrication follows the RIBAE process using a Kaufman & Robinson 14 cm RF-ICP ion beam source. RIBAE parameters are: 200 V beam potential, 26 V accelerator potential, 85 mA beam current, ~155 W ICP power, 37 sccm O₂ flow rate, and 7.5×10^{-4} Torr process pressure. A non-immersed electron source neutralizer is used to neutralize positive ions from the beam. The neutralizer is mounted on the side of the ion source with the emission current set to 1.25x of the ion source beam current, and with an Ar gas flow of 10 sccm.

Top-down RIBE of the sample is performed to achieve the desired depth of the structures followed by removal of the HSQ mask via hydrofluoric acid (HF). Nb does not react with HF, leaving the Nb mask intact to serve as the mask for the angled-etching process. The reasoning for the 70 nm-thick Nb mask is two-fold. First, it is an excellent etch mask for oxygen plasma, providing ample selectivity to create the desired structures without significant mask erosion. Second, a thin mask is required such that when the sample is tilted, the height of the resist should not shadow neighboring nanostructures. This restriction puts an ultimate limit to how close patterns can be relative to each other (i.e. this restricts the pitch) while still allowing undercut columns to be created.

RIBAE is performed at the design angle α (e.g. 70°) until the desired undercut is achieved and the target column dimensions are realized. This is followed by the removal of the Nb mask using buffered chemical polish (BCP) which consists of two parts 85% phosphoric acid to one part 49% hydrofluoric acid to one part 70% nitric acid. The sample is then rinsed in deionized water, followed by a solvent clean with acetone and isopropyl alcohol. The key characteristic of this technique is the remarkable uniformity across a wide area, potentially as large as 200 mm in diameter, limited only by the size of the ion beam source used.

Experimental setup for reflection spectrum and beam profile measurements. The reflection spectrum of a diamond mirror is measured using the setup outlined in Extended Data Fig. 2. Broadband light is generated using a 1065 nm superluminescence diode (SLD) (InPhenix IPSDD1004C), is collimated and directed, using broadband silver mirrors (Thorlabs PF10-03-P01), to a 50:50 beamsplitter (Thorlabs CM1-BP145B3) after passing through a lens (Thorlabs AC254-300-C-ML) which focuses the beam at the diamond mirror (or reference mirror, see below). Reflected light is directed by the beamsplitter to an identical lens that collimates the beam and directs it to an optical spectrum analyzer (Yokogawa AQ6370). We use a lens of long (300 mm) focal length to ensure the diameter of the beam at the diamond mirror is less than 1 mm, which is much smaller than the patterned area on the diamond crystal (3 mm x 3 mm). After a spectrum of a broadband silver mirror (Thorlabs PF10-03-P01) is measured for reference, the diamond mirror is measured, and its spectrum is determined with normalization to the reference.

A more precise measurement of reflectivity at 1064 nm is performed by replacing the SLD with a 1064 nm distributed Bragg reflector (DBR) laser of 10 MHz linewidth (Thorlabs DBR1064S) and the optical spectrum analyzer with a free-space optical photodetector (Newport 918D-SL-OD3R sensor attached to a Newport 1936R power meter, averaging mode). A reference measurement is taken using a Nd:YAG laser and a mirror of 99.8% reflectivity (Thorlabs NB1-K14) to precisely determine the reflectivity of the diamond mirror at 1064 nm.

Beam profile measurements are performed using the 1064 nm DBR laser with a scanning slit beam profiler (Thorlabs BP209-IR) replacing the photodetector. A least-squares method is used to fit the x-y cross-section profile of the beam, see Fig. 3B.

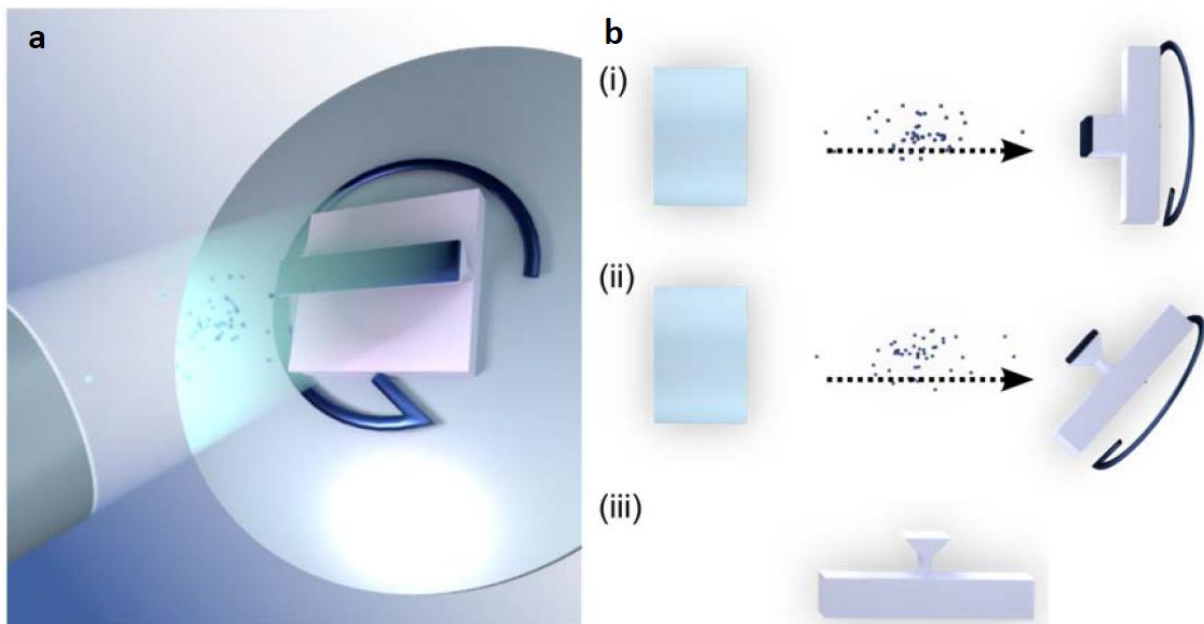
Setup and details of laser damage testing experiments. The laser-induced damage threshold (LIDT) tests of the diamond and dielectric mirrors are assessed at the Pennsylvania State University Applied Research Laboratory, Electro-Optics Center. The testing is performed using a 1070 nm multimode fiber laser from IPG Photonics, capable of providing up to 10 kW of continuous wave laser light. The diamond mirror is designed and fabricated to reflect light of 1070 nm wavelength and is clamped to a water-cooled aluminum stage (Aavid 416401U00000G) using Cu clamps. The dielectric mirror (Thorlabs BB2-EO3) is also mechanically clamped to the water-cooled aluminum stage. The chiller used to cool the stage is at a temperature of 18°C and flows at approximately 7.5 liters per minute. A lens of 500 mm focal length focuses the laser to a spot of $750\ \mu\text{m}$ ($1/e^2$) diameter at the diamond and dielectric mirrors. Inspection and digital image capture of the mirrors are performed during the LIDT tests using an off-axis optical camera. A FLIR thermal imaging camera is also used to monitor the temperature of the mirrors and aluminum stage throughout testing. It is directed $2\text{-}3^\circ$ off normal incidence to avoid reflections returning into the laser.

The reflection spectrum of the diamond mirror is simulated and measured beforehand using the superluminescent diode and accompanying setup as described in the previous section, with results shown in Extended Data Fig. 3, noting the reflectivity is 96% at 1070 nm. The spectrum of the 10 kW IPG laser is also shown in this figure (in arbitrary units), illustrating the overlap of the laser used during LIDT testing with the reflection spectrum of the diamond mirror under test.

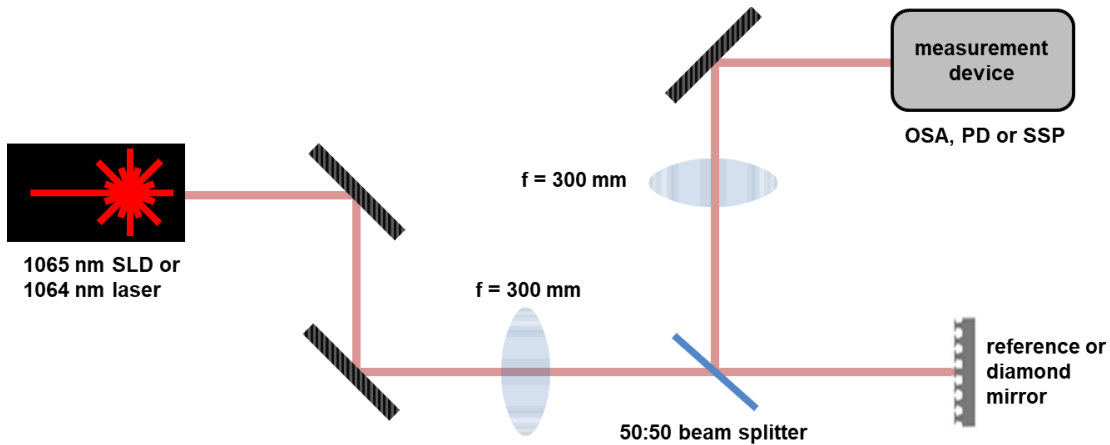
The cross-section profile of the high-power beam from the IPG laser is measured using a Primes focus monitor, results are shown in Extended Data Fig. 4 along with a Gaussian fit. The Primes focus monitor has a metal tip with a pinhole of 20 μm diameter that can be translated by a motorized stage to the desired location. The tip traverses the entire area of the beam, collecting a 2-D map of the beam profile.

The LIDT test is performed such that the mirrors are irradiated for 30 s with a constant laser power. The laser power is increased from 0.5 to 10 kW, and the test is repeated for each power level, see the caption of Fig. 4. During each LIDT test of the diamond and dielectric mirrors (i.e. for each power level), the temperature at the hot spot quickly reached a steady state once illumination began, and remained at that temperature until illumination ceased. That is, except for the 10 kW-test using the dielectric mirror, i.e. at the onset of damage of the dielectric mirror. The steady-state temperatures are shown in the thermal images of Figs. 4B-E and 4H-J. As illustrated in these figures, the hot spot temperature rose more quickly with increased laser power during the dielectric tests (see next paragraph). However, the temperature of the hot spot for the 10 kW tests of the dielectric mirror did not reach a steady state, but steadily increased over the duration of illumination until damage ensued, at which point the laser illumination was halted. The image in Fig. 4K is taken immediately after damage occurs.

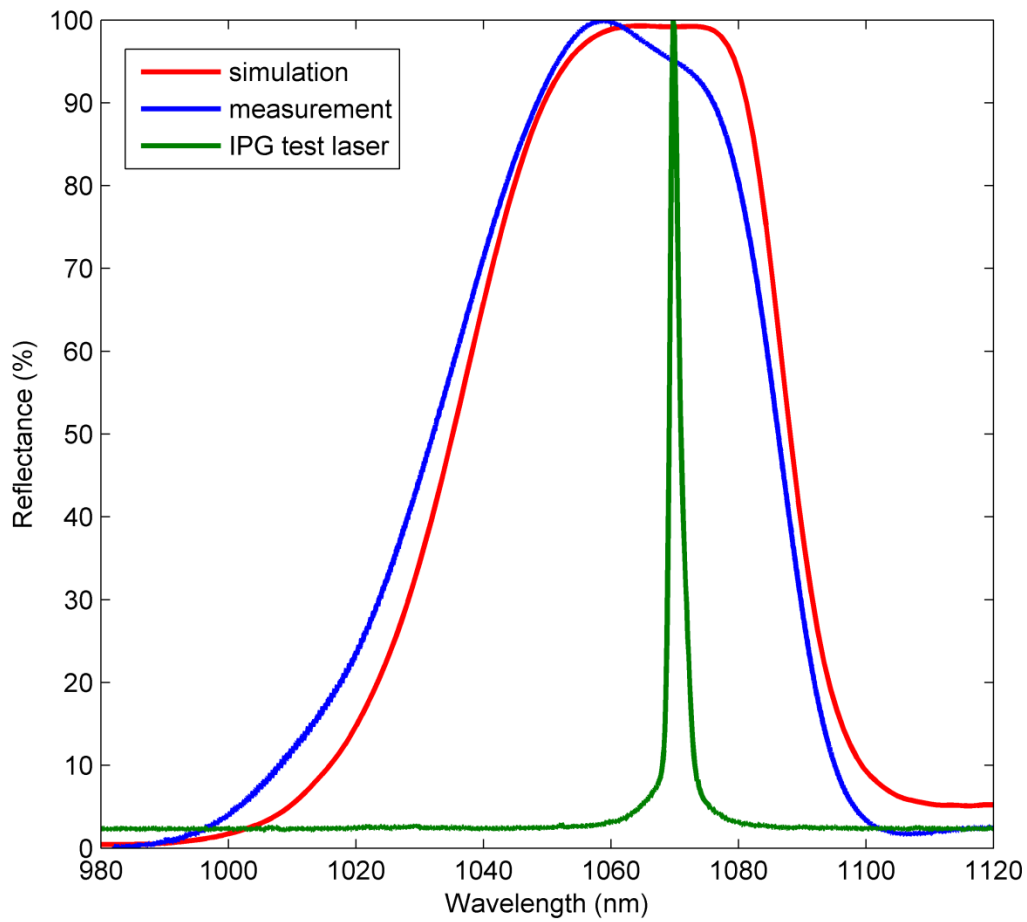
As widely discussed in literature¹⁵, the relatively low thermal conductivity of commonly used substrates and coatings for dielectric mirrors, led to the rapid temperature increase of the laser exposure site. Combined with the high, and varying, thermal expansion coefficient of these coatings, thermal stress resulted, and subsequent damage occurred. In contrast, tests of the single-crystal diamond mirror, which has high thermal conductivity, led only to heating of the aluminum plate, and no damage.



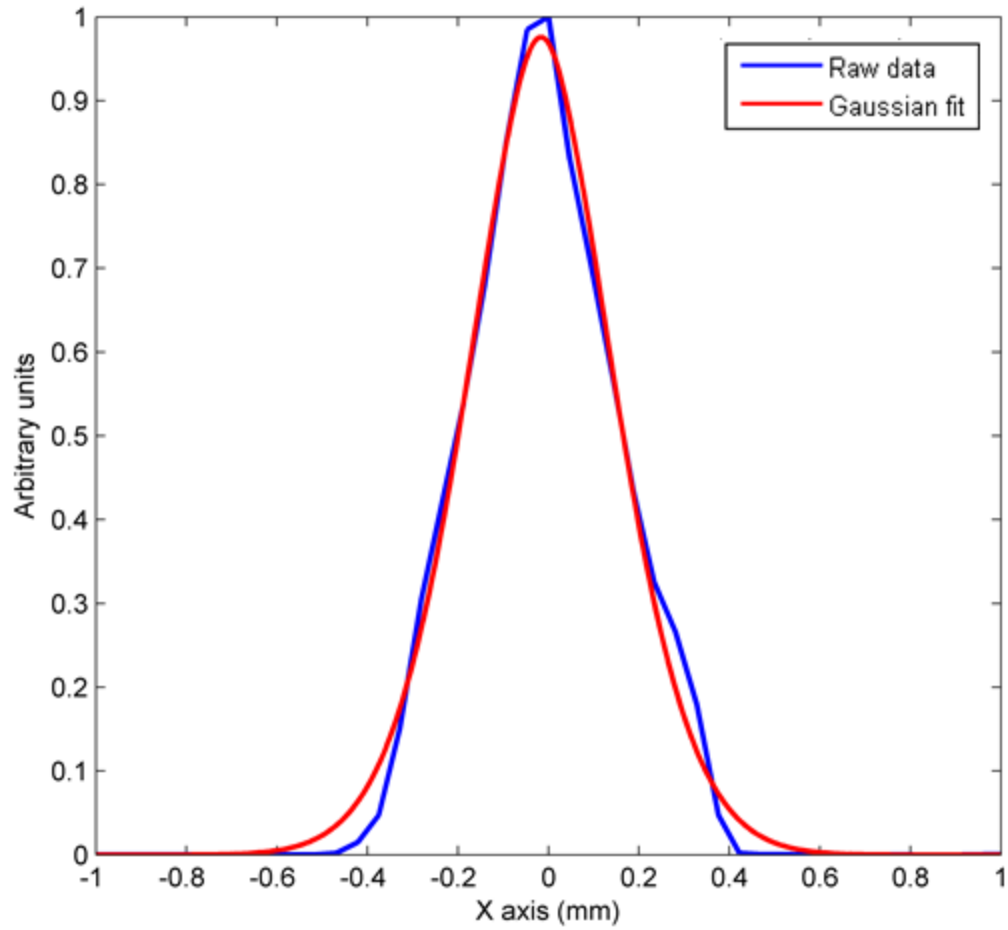
Extended Data Fig. 1 | Reactive ion beam undercut etching (RIBAE). **a**, Graphical depiction of RIBAE. **b**, RIBAE fabrication steps (i) Top-down etching of a diamond sample mounted perpendicular to the ion beam path on a rotating sample stage. (ii) Sample is tilted to obtain an acute angle between the sample and ion beam, uniformly etching underneath the etch mask. (iii) Mask removal yields undercut nanostructures from a bulk substrate.



Extended Data Fig. 2 | Schematic of the experimental setup used for measuring the reflection spectrum of a diamond mirror and beam profile measurements. The reflection spectrum is measured using light from a 1065 nm SLD that is collimated and directed with broadband silver mirrors to a 50:50 beamsplitter after passing through a focusing lens. Reflected light from the diamond mirror, or a reference mirror, is directed to an optical spectrum analyzer (OSA) after passing through a defocusing lens. A 1064 nm DBR laser source and free-space optical photodetector (PD) replaced the diode and OSA for the more precise reflectivity measurements. The PD was replaced by a scanning slit profiler (SSP) for beam profile measurements.



Extended Data Fig. 3 | Reflection spectrum of the diamond mirror used for LIDT measurements at 1070 nm. A diamond mirror measured (blue curve) and simulated (red curve) reflection spectrum at normal incidence. Green curve shows the spectrum of the 10 kW IPG laser used during damage testing plotted in arbitrary units.



Extended Data Fig. 4 | Beam profile of 1070 nm IPG LIDT test laser. Beam profile is collected using a Primes focus monitor. The focus monitor has a metal tip with a 20 μm -diameter pinhole in the side. The rotating tip then traverses the entire area of the beam, collecting 2-D data of the beam profile. Blue line represents the raw data from the x-axis of the beam. The red line is the Gaussian fit.